Transport in Porous Media **11:** 161–177, 1993.

Pore Structures and Transport Properties of Sandstone

C. DAVID, M. DAROT
EOPGS Laboratoire Matériaux, 5 Rue Descartes, 67084 Strasbourg Cedex, France

and

D. JEANNETTE
CGS, 1 Rue Blessig, 67084 Strasbourg Cedex, France

(Received: 22 May 1991; in final form: 2 March 1992)

Abstract. We report laboratory measurements of pore structure, capillarity, water permeability, and electrical conductivity on Fontainebleau sandstone specimens. Experimental equipment and techniques are described. Water permeability measurements were performed on saturated cores with a 100 MPa permeameter. Various combinations of pore and confining pressures were used and an effective pressure law was determined. In addition, electrical conductivity of samples saturated with KCl brines was measured over a wide range of electrolyte conductivities (10^{-3} to 1 S m^{-1}). The well-known relationship $F = \Phi^{-m}$ fits well our data, and empirical parameters such as the cementation exponent and tortuosity factor are derived. Differences between transport properties of the three types of sandstone are related to the microstructural characteristics of the pore network of each rock.

Key words. Sandstone, pore structure, porosity, permeability under confining pressures up to 100 MPa, electrical conductivity.

1. Introduction

The transport properties of rocks are of major interest and many studies on sandstones as well as on crystalline rocks can be found in the geophysical literature (Brace, 1980; Brace and Orange, 1968; Brace *et al.*, 1965, 1968; Daily and Lin, 1985; Doyen, 1988). These properties are controlled by porous network characteristics. In particular, permeability, capillarity, and electrical conductivity depend on the structure of the connected porosity. Interpretations of experimental data on these properties in terms of microstructural parameters are not common; it seems, however, a very attractive approach.

In this paper, we describe the high pressure permeameter which simulates *in-situ* pressure conditions. Then we report permeability measurements versus pore and confining pressures, electrical conductivity, porosity, and capillarity data on three types of Fontainebleau sandstone. A thorough analysis is conducted on thin sections of specimens prepared by epoxy injection or imbibition. Precise information on the microstructure of the porous networks is related to the variations of the measured transport properties.

2. Experimental Equipment and Techniques

2.1. TESTING PERMEAMETER

The experimental apparatus has three main parts, namely the pressure cell, the confining pressure system, and the pore pressure system (Figure 1). The maximum pressure capability is 100 MPa; every combination of pore pressure and confining pressure in the range 0.1–100 MPa can be obtained. The versatility of the apparatus was one of the major design constraints. Permeability measurements can be performed with liquids or gas. We used water in our experiments. Special attention was given to the pore pressure system, since further experimental developments will require the use of strong electrolytes as pore fluids. In particular, the pore pressure tubing is restricted to a minimum length to reduce corrosion problems. For the same reason, a water/electrolyte separator may be added in the pore pressure line. In this configuration, the electrolyte is insulated from the water regularly used as a pressure medium in the hand pump. Special constant volume valves (compensated valves)

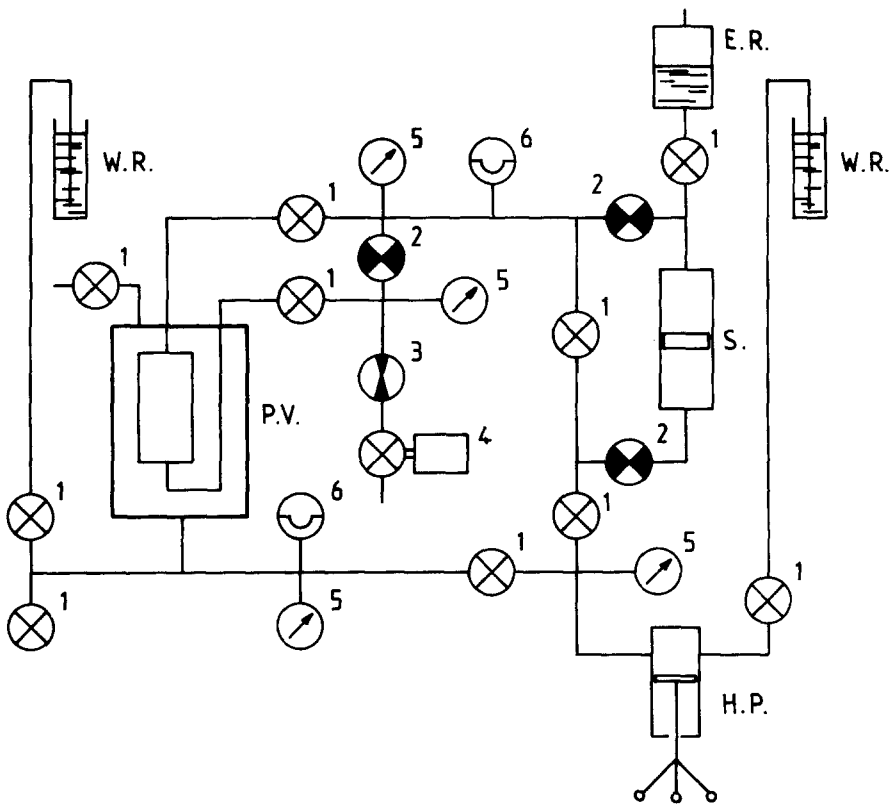

Fig. 1. Schematic drawing of the permeameter. (1) regular valve, (2) compensated valve, (3) metering valve, (4) valve with air operated actuator, (5) pressure transducer, (6) rupture disc, E.R. electrolyte reservoir, H.P. hand pump, P.V. pressure vessel, S water/electrolyte separator, W.R. water reservoir.

have been designed to allow us to close a circuit without altering its pressure (i.e. without pressure increase at the closure). Absolute pressure transducers are used to measure the hand pump pressure, the confining pressure, and both upstream and downstream pressures (0–100 MPa, $\pm 0.2\%$). A special conditioning module gives the differential pressure between upstream and downstream pressures (0–0.7 MPa, $\pm 0.5\%$).

The samples are cores drilled to 20 mm in diameter and ground square to a length of 40 mm. They are protected by a polyurethane rubber jacket and clamped on end plugs. This sample assembly is hang inside a large stainless steel tube (2 mm thick wall) attached to the top plug of the pressure vessel (Figure 2). The top end plug (upstream end plug) is fixed on this tube while the bottom one (downstream end plug) may slide upwards and downwards without rotation. A bolt with a central finger maintains the bottom plug in contact with the specimen.

The testing apparatus allows permeability measurements by two methods, in a steady-state mode and in a transient mode. In the steady-state mode, the permeability K (in m^2) is given by Darcy's law:

$$K = \frac{\mu L \, \Delta m}{\rho A \, \Delta P \, \Delta t},$$

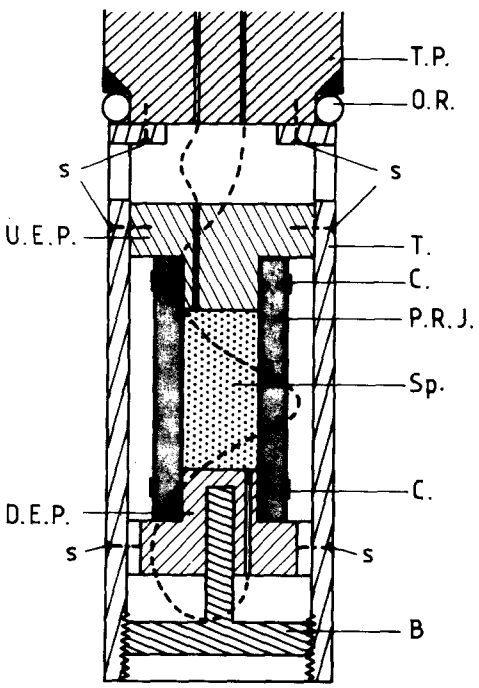

Fig. 2. Sample assembly. B. bolt with centering finger, C. clamp, D.E.P. downstream end plug, O.R. O Ring, P.R.J. polyurethane rubber jacket, S. screw, Sp. specimen, T. 2 mm wall thick stainless stell tube, U.E.P. upstream end plug, Dashed lines: pore pressure tubings.

where Δm is the mass of pore liquid flowing through the sample during the time Δt of the measurement, μ and ρ are, respectively, the viscosity and the mass per unit volume of the pore liquid, L and A are the length and the cross-section area of the specimen, ΔP is the pressure gradient along the specimen (upstream and downstream differential pressure). The confining and differential pressures are displayed on digital indicators and recorded on a chart recorder. The mass flow rate is measured with electronic scales which are sampled versus time by a personal computer. Data are displayed on a X-Y plotter. Darcy's law implies a laminar flow with a constant pressure gradient ΔP. This means that the flow rate must be constant and, thus, the X-Y plot of the mass versus time must be a straight line. In the steady-state mode, the permeability measurements may range from 10^{-2} to 10^{-6} Darcies (1 Darcy $= 10^{-12}$ m^2). The uncertainty varies from 10% for high permeabilities to 5% for low permeabilities.

When the mass flow rate (in the steady-state regime) is too low and, thus, the time required for measurements too long, another method must be used. In the transient mode, a pressure pulse is applied at one end of the specimen, and the pressure relaxation through the specimen is recorded versus time; the pressure decay rate is related to the permeability. This technique is suitable for very low permeability measurements and is more appropriate to crystalline rocks; thus the steady-state mode was used on sandstones specimens.

2.2. ELECTRICAL CONDUCTIVITY DEVICE

Specimens are cores prepared the same way as for permeability measurements. When the final geometry is obtained, samples are carefully washed out with deionized water to remove the water soluble grinding solution from the porous network. This operation is critical since the solution is highly conductive. The absolute purity of the specimen is ascertained by recording the electrical conductivity of the cleaning water. Several hours may be needed to bring the conductivity back to the deionized water value (150 μS m^{-1}). Next, specimens are dried at 80°C for two hours. A silicone jacket is fitted tightly on cores and the jacketed specimens are then put under vacuum ($\cong$10 Pa) at least for 2 h. Saturation of samples is obtained with degassed electrolyte water solutions, specimens are left for 48 h in brine prior any electrical measurements.

The experimental set-up is shown in Figure 3; each end of the specimen is covered with a disc of filter paper soaked in KCl solution. Then the specimen with end discs is set between the two electrodes. The electrode holder can slide to the right and left and be clamped in such a position as to fix the applied force at a constant value, whatever the length of the specimen. This is achieved by using a gauge which determines the 'constant' length of the compression spring. Electrical conductivity measurements are made with a WTW LF2000 conductivity meter at a fixed frequency (4 kHz) at room temperature and pressure. They yield the well-known

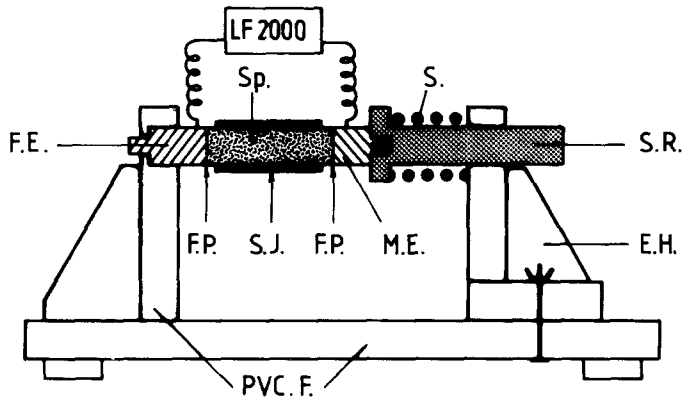

Fig. 3. Electrical conductivity bench. E.H. adjustable electrode holder, F.E. fixed electrode, F.P. filter paper disc, LF 2000. conductivity meter, M.E. mobile electrode, PVC. F. polyvinyl chloride frame, S. compression spring, S.J. silicone jacket, Sp. specimen, S.R. PVC sliding rod.

formation factor F, and in addition they allow us to estimate the importance of surface conductivity processes in samples saturated with conductive electrolytes.

2.3. CAPILLARITY TESTS

The porous network of a rock is first quantified by its overall volume. A measurement of the total pore volume (Nt) is given by the volume of water invading a specimen under vacuum (Monicard, 1975); Bousquié, 1979). Similarly, the imbibable pore volume accessible to water by capillarity can be measured from water imbibition experiments under gradual immersion over 48 h (N48). The difference Nt-N48 (Pickell *et al.*, 1966) gives the pore volume with trapped air which corresponds to the volume occupied by the less wetting phase (air) after the completion of a capillary imbibition experiment.

In a first approximation, during a capillary imbibition experiment, water flow (wetting phase) within the sample is controlled by the narrowest throats of the porous network. If the amount of water provided by the narrow 'filling' channel of a large pore is too small, water may progress as a film along the rough walls and reach the top of the bulge, leaving inside an undisturbed volume of air. Consequently, a portion of the volume of large pores remains occupied by the nonwetting phase (air), whereas the imbibable pore volume, generally composed of smaller pores, is entirely invaded. As the velocity of permeating water in capillary depends on its cross-section, imbibition kinetics of a sample may reflect the properties of the porous network; in particular, it may give some insight into the pore size distribution.

According to Washburn's equations derived from Poiseuille's law and capillary pressure, the water height in a capillary tube is proportional to the square root of time: $h \propto t^{1/2}$, the water volume and consequently the water mass is proportional to this height $w \propto h$, hence $w \propto t^{1/2}$. Experimental data on the distance of migration of the imbibition front and on the water mass increase are both plotted versus the

square root of time. For a specimen with an homogeneous porous network and with a limited length, data points of both front migration and mass increase form straight lines as long as they correspond to imbibition of the imbibable pore volume (free porosity). The relative positions of these straight lines and their slopes make it possible to estimate the homogeneity of the imbibable pore volume network. In addition, comparison of the size of interconnections between large pores can be made on specimens of similar petrographic nature.

2.3. VISUALIZATION OF THE PORE STRUCTURE

Numerous techniques of pore structure study are available (Dullien and Dhawan, 1974; Wardlaw and Taylor, 1976; Dullien, 1979). Measurements of the total pore volume does not give any information on the structure of porosity (i.e. pore distribution, localization of pores with respect to the different minerals). The porosity structures are studied on thin sections of sandstones injected with coloured epoxy (Zinszner and Meynot, 1982). There are two different types of thin sections. The first one is made from rocks injected with epoxy under vacuum and then, under pressure. During this process all the interconnected pores larger than 0.1 μm are occupied. In the second type, specimens are not outgassed, the imbibable porosity is filled with red epoxy, and the porosity occupied by air is then filled by spreading blue epoxy on the cut surfaces. The porous volume accessible to epoxy under vacuum and then under pressure, and the volume invaded by water under vacuum are nearly identical. However, during double coloration process, the pore volume filled with epoxy by capillarity in air depends on epoxy viscosity: 15×10^{-3} Pa s. As water viscosity is 10^{-3} Pa s, the porosity volume invaded by red epoxy is smaller than the volume accessible to water. Both imbibable pore volume and pore volume with trapped air are determined by a usual point-counting method on coloured thin-sections. In addition, measurements, under the microscope of the largest pore diameters (Friedmann, 1958), gave access to the pore size distributions of imbibable pores and pores with trapped air. The accuracy of these determinations depends on two main factors: (1) the sharpness of the pore limits (the pore contours may often look fuzzy because of the thin section thickness) and (2) the resolution of the microscope itself which does not allow determination of pore size smaller than 2 μm, and even more often, 5 μm. These limiting effects are critical when the pore size is small and the porosity is low. However, the study of porous media under the microscope makes it possible to determine the behaviour of macropores during imbibition together with their size and their location with regards to the different minerals. The anisotropy as well as the continuity of the porous network can also be studied. All these microstructural investigations lead to correlate transformations in the porous structures with transformations in minerals, and to gain a better understanding of the variation of transport properties (Mertz, 1989).

3. Experimental Results

3.1. MATERIAL AND SAMPLE DESCRIPTION

Fontainebleau Sandstone is a pure sandstone found in the Ile-de-France region south of Paris. It was chosen for its petrographic purity since it is composed of more than 99% quartz; furthermore it is a well-sorted sandstone. However, as the degree of silicification differs from one sample to another, the bulk porosities and the characteristics of the porous networks show a wide range of variation (Bourbié *et al.*, 1986).

Sample No. 1 (S1) consists in a quartzitic sandstone with a fairly constant grain size (150–300 μm). As is all Fontainebleau sandstones, detritic grains are ovoid and rarely surrounded by iron oxide and hydroxides. Contacts between grains are almost tangential and the remaining intergranular spaces are partially filled by overgrowth rings of quartz with well developed crystalline faces (Figure 4). The assemblage of these euhedral quartz grains is not perfect and includes large pores with rectilinear contours (Figure 5). Patches of dissolution sometimes appear, and overgrowth rings, or even detritic grains, may show corrosion features. This results in an enlargement of pores which no longer show polygonal shapes but rather cuspate or concavo-convex contours. In thin section, the porosity appears as an angular network of channels; the mean length of the channel is of the order of the grain size (up to 300 μm), the width ranges from 30 to 110 μm but widths between 100 and 200 μm are encountered regularly (mean grain size spacing). When they are limited by the flat faces of euhedral grains, they show typical polygonal shapes (Figure 6). Sometimes, larger pores may be found; they are caused by dissolution and have irregular shapes. On bicoloured thin sections, the trapped porosity is localized in the largest pores (Figure 6) whatever their shapes. By contrast, imbibable pore volume occupies both

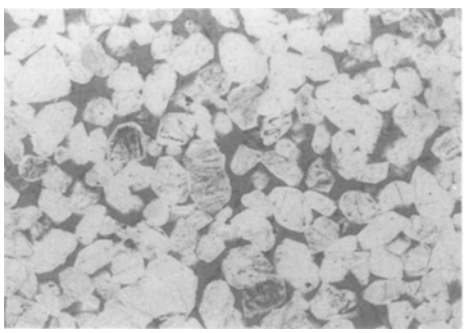

Fig. 4. Structure of porosity of sample No. 1 after vacuum/pressure injection of red epoxy (here in medium grey). Large primary pores have angular contours; Larges pores with irregular smooth shapes result from dissolution. Height is 1.6 mm.

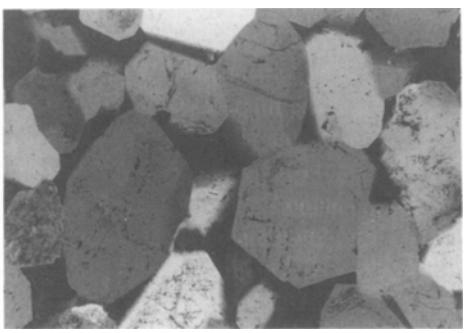

Fig. 5. Same as Figure 4. Overgrowth rings transformed detritic grains (outlined by inclusions) into euhedral grains. Crossed nicols slightly off. Height is 0.8 mm.

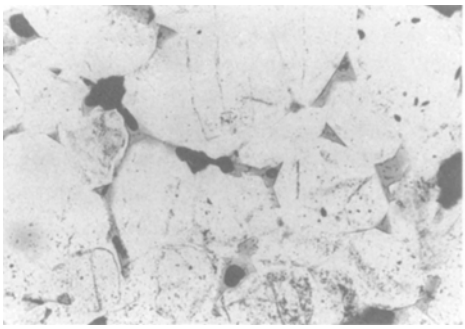

Fig. 6. Bicoloured porosity of sample No. 1. Imbibable pore volume consists in angular pores, in medium grey (red epoxy), with interconnecting channels. Trapped porosity occupies the largest pores, in black (blue epoxy). Height is 0.8 mm.

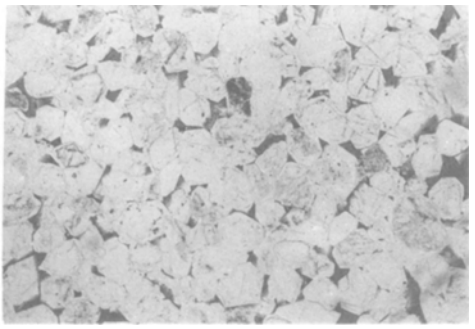

Fig. 7. Structure of porosity of sample No. 2 after vacuum/pressure injection of red epoxy (medium grey). Primary pores are smaller than in sample No. 1 (Figure 6). They seem not to be interconnected at this scale. Height is 2 mm.

small dilations with polygonal shapes and a whole set of channels forming a continuous network visible throughout all of the thin sections. Examination of several thin sections shows an homogeneous porous network with no predominating pore size family. Moreover, no particular porous or clogged zones are identified.

Sample No. 2 (S2) is composed of smooth and regular quartz grains (120–225 μm) surrounded by well developed overgrowth rings. The main geometrical features of the porous network are very similar to sample S1 characteristics. Differences lie in the dimensions and in the distribution (Figure 7). On the thin section with coloured porosity (vacuum/pressure injection), the pore size ranges from

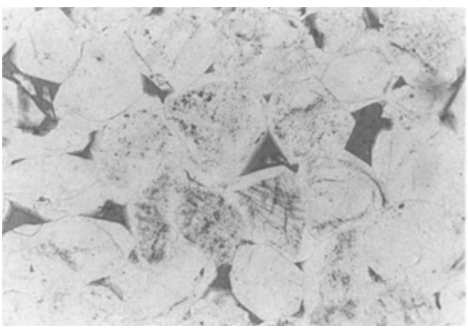

Fig. 8. Same as Figure 7. Geometrical pores are delineated by overgrowth rings. Free porosity consists mainly of polygonal pores connected by very narrow channels hardly decorated by red epoxy. Height is 0.8 mm.

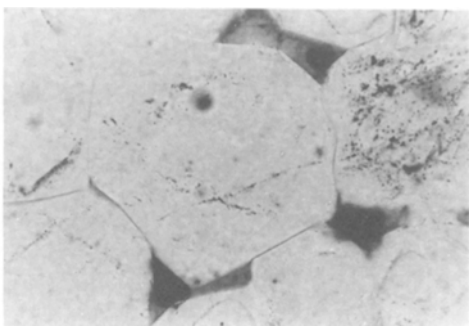

Fig. 9. Bicoloured porosity of sample No. 2. Imbibable pore volume is represented by angular pores in medium grey (red epoxy). 'Filling' channels, when visible, appear as thin lines at the grain boundaries. Trapped porosity is represented by rounded black (blue epoxy) patches inside free pores. Height is 0.4 mm.

50 to 100 μm (Figure 8). On bicoloured thin sections, the pore volume with trapped air is very large and occupies all large pores. The only imbibable pores visible are smaller than 50 μm. Imbibable pores with polygonal shapes are hardly ever found in the thin sections. Interconnecting feeding channels, through which epoxy permeated, are not visible (Figure 9). This means that their width is below the resolution of the microscope (<2 μm).

Sample No. 3 (S3). consists in a silicified sandstone without secondary dissolution; it appears as a compact stacking of quartz grains (50 to 350 μm grain size) in which extensive overgrowths give rise to denser areas of various sizes. The main feature of this sandstone is its heterogeneity which can be analysed even at the scale of the thin sections. In fact, within a few hundreds microns, one may encounter a silicified zone with no porosity as well as a large pore area.

3.2. POROSITY AND CAPILLARITY DATA

The bulk porosity of specimen S1 is 12.3%, the imbibable pore volume is 5.7% and hence the pore volume with trapped air is 6.6%. Measurements, under the microscope, of the largest dimension of pores are plotted on a frequency diagram (Figure 10). The median is 124 μm which is close to the limit between the largest free pores and the smallest trapped pores. This emphasizes the importance of large pores in the imbibable pore volume. The steep slopes of capillary curves (water mass increase and imbibition front migration) on Figure 11 reveal a rapid capillary imbibition and therefore suggest not only the existence of a subnetwork of large pores, but the presence of an almost unique family of pore diameter. The whole imbibition is reached when the water front reaches the top of the sample; this argues for an homogeneous distribution of free pores throughout the sample.

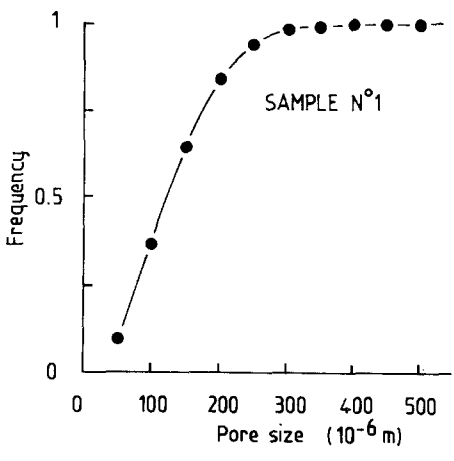

Fig. 10. Cumulative pore size distribution of sample No. 1.

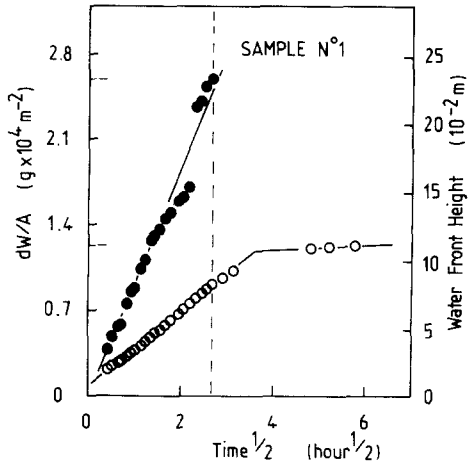

Fig. 11. Capillarity curves of sample No. 1. -solid circles water mass increase versus time -empty circles water front height versus time.

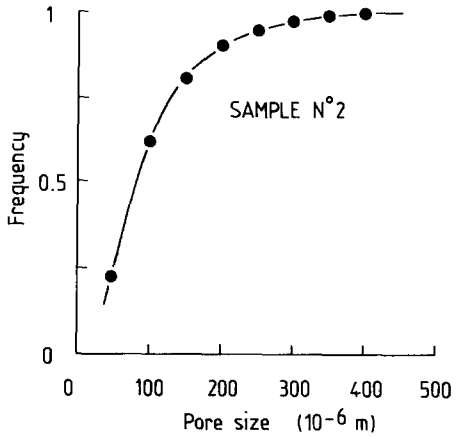

Fig. 12. Cumulative pore size distribution of sample No. 2.

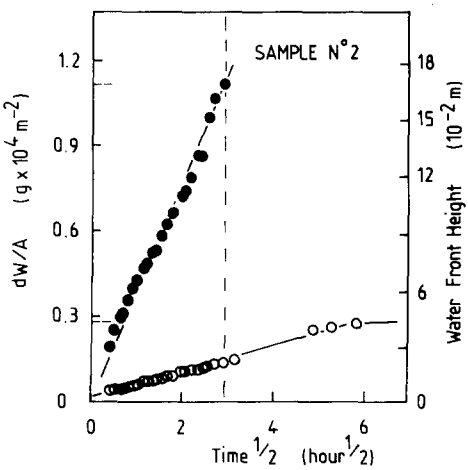

Fig. 13. Capillarity test curves of sample No. 2. –solid circles water mass increase versus time – empty circles water front height versus time.

The bulk porosity of specimen S2 is 6.0%, the imbibable pore volume is 1.6%, and by difference, the pore volume with trapped air is 4.4%. The analysis of the pore size distribution (Figure 12) indicates that the largest imbibable pores are below the lower quartile. This reveals that all of the imbibable pore volume is composed of small pores. Capillary curves give some information on the pore size distribution. On Figure 13 the low value of the slope of the water mass increase curve is interpreted as a consequence of the narrowness of imbibable pores. In addition water needs much more time to saturate the whole porosity than to reach the top of the specimen by capillarity. This fact supports the argument of heterogeniety in the distribution of the imbibable pores. In fact, wetting of the specimen corresponds to the rapid imbibition of the largest and best interconnected imbibable pores, up to the top of the specimen. Furthermore, free porosity imbibition develops by filling a sub-network composed of irregular pores interconnected by narrow channels.

The bulk porosity of sample S3 is around 5.1% with 1.5% imbibable pore volume, the resulting pore volume with trapped air is then 3.6%, which represents 70% of the bulk porosity. This large relative value is well illustrated in thin section with coloured porosity since nearly all visible pores belong to the pore volume with trapped air. Rare exceptions are found in small imbibable pores ($<30\,\mu m$). The network of the imbibable pore volume seems discontinuous, which may be due to the resolution of the optical microscope. It may also be the reality since silicification is widespread and hence connectivity is low. On the pore size diagram in Figure 14, the pore size of imbibable pores falls below the lower quartile of the population. Heterogeneity is so high and connectivity so low that, in spite of several trials, no regular imbibition test could be performed (Figure 15).

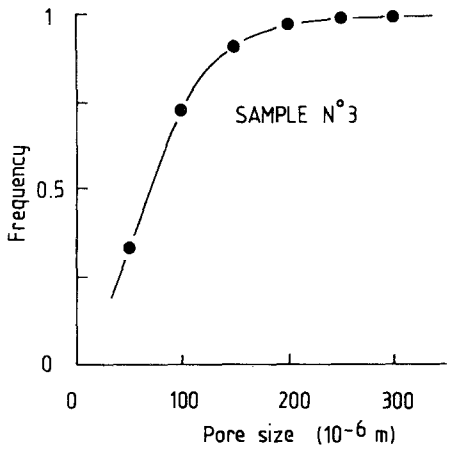

Fig. 14. Cumulative pore size distribution of sample No. 3.

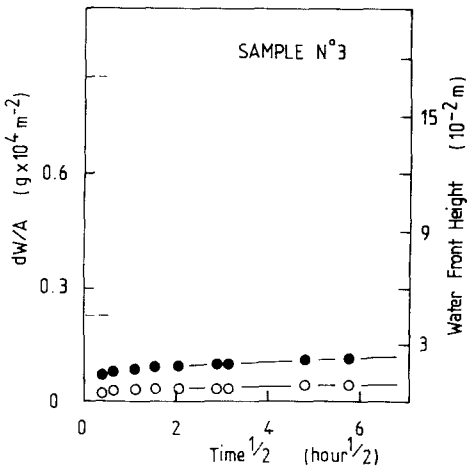

Fig. 15. Capillarity test curves of sample No. 3. –solid circles water mass increase versus time – empty circles water front height versus time.

3.3. PERMEABILITY MEASUREMENTS

Permeability measurements were made in the steady state mode over a wide range of pressure conditions. The same experimental procedure was applied to each sample. First, the confining pressure was increased to a given value, and then permeabilities were measured at increasing pore pressure levels. As the measurements are only made when pressure equilibrium is reached, this type of experiment is time-consuming. For example, it took several weeks to assemble the data of Figure 17.

Figure 16 gives a plot of water permeability versus confining pressure for sample No. 1 at a constant value of the pore pressure (10 MPa). The decreasing trend of permeability measurements is almost linear. At the highest pressure (80 MPa), Sample No. 1 lost more than 60% of its permeability value at 20 MPa confining pressure.

Compared to sample No. 1, sample No. 2 shows a rather different behaviour. In Figure 17, permeability evolution with confining pressure is plotted at given pore

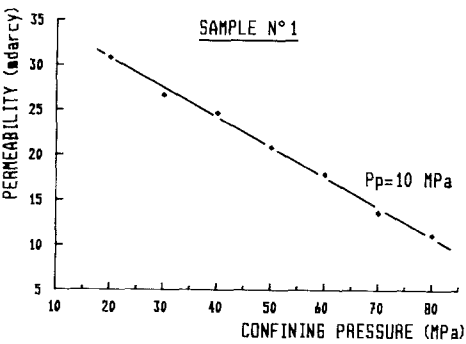

Fig. 16. Permeability vs. confining pressure at 10 MPa, sample No. 1.

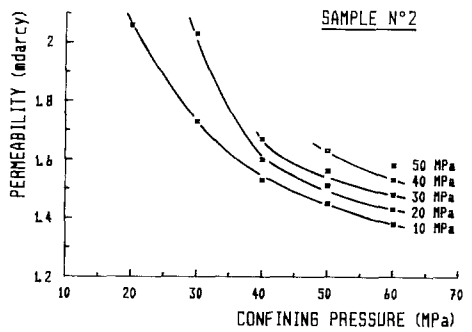

Fig. 17. Permeability vs. confining pressure at given pore pressures, sample No. 2.

pressures. It is no longer linear, this diagram shows a large permeability decrease in the low confining pressure range. At 10 MPa pore pressure, the permeability loss is about 70% over the whole confining pressure range. This fast decreasing trend at low pressure can be explained by the closure of low aspect ratio pores (i.e. ratio of the smallest to the largest dimension of a pore). As a consequence, it seems likely that the porous network connectivity was greatly reduced in the first part of our experiments. Furthermore, irreversible changes in the pore structure took place during confining pressure cycles. This is illustrated by permeability measurements; indeed, values measured in the increasing phase of a confining pressure cycle are always larger than those in the decreasing phase.

Figure 18 shows another important feature of our data relative to Sample No. 2. Permeability data plotted as a function of pore pressure exhibit linear trends for each given confining pressure. Compared to what is shown on Figure 17, this indicates that pore pressure and confining pressure do not play symmetrical roles in the deformation of this sandstone. Confining pressure when applied outside the jacketed sample is transmitted to the pores via the solid skeleton of the quartz grains. It is likely that stress concentrations develop during confining pressure increases, giving rise eventually to some microcracking or grain reorganization. There is indeed a departure from hydrostatic state of stress. However, the pore pressure seems to act effectively as an internal hydrostatic stress resulting in a linear response.

All the permeability measurements for Sample No. 2 are consistent with the effective pressure concept. The effective pressure P_{eff} is defined as the confining pressure which, applied alone (at zero pore pressure), would yield the same permeability as observed for a given combination of confining and pore pressure (Bernabé, 1987). Plotting the permeability K in the (P_c, P_p) coordinates, the family of

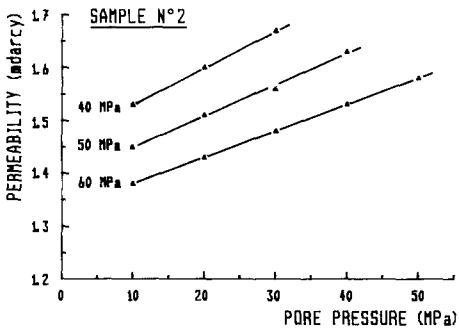

Fig. 18. Permeability vs. pore pressure at given confining pressures, sample No. 2.

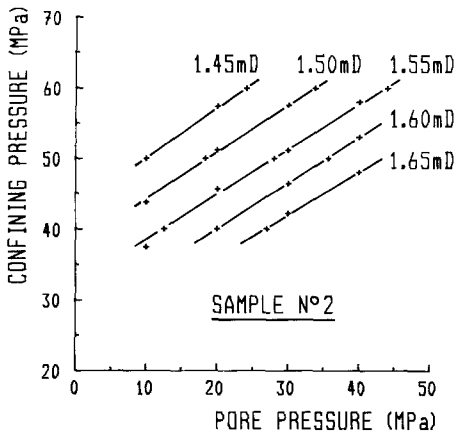

Fig. 19. Confining pressure-pore pressure plot of isopermeability curves, sample No. 2. Crosses are obtained by interpolations on our experimental data at given permeability values.

curves $K(P_c, P_p)$ = constant provides the means of estimating effective pressure laws relating P_{eff} to P_c and P_p. In Figure 19, equal permeability curves are straight lines, thus they define an effective pressure law of the form:

$$P_{\text{eff}} = P_c - \alpha P_p, \quad \alpha \leqslant 1$$

where the α coefficient is determined by the slope of the isopermeability straight lines in the (P_c, P_p) plane.

Some analytical expressions have been calculated for the effective pressure coefficient α; for example, Nur and Byerlee (1971) in their study of the elastic compression of porous rocks, related to the bulk moduli of the porous medium and the material of which the rock is composed. However, as suggested by Robin (1973), the effective pressure law is not unique but varies with the physical property involved. Therefore, it is necessary to determine experimentally the effective pressure law relatively to the permeability. For Sample No. 2, the α coefficient ranging between 0.60 and 0.75, is in good agreement with other studies on the transport properties of rocks (Bernabé, 1987, 1988). Furthermore, α is found to increase slightly with increasing confining pressure (or decreasing permeability).

As α estimates the relative efficiency of pore pressure compared to confining pressure, we conclude that, according to our data, pore pressure is more efficient in the high confining pressure region. It seems that as soon as the closure of the 'weakest' fraction of the porosity is obtained, the deformation of the porous network becomes more and more sensitive to internal pressure. This increased sensitivity remains, however, moderate and α does not increase up to 1. This result differs from Bernabé's observations on crystalline rocks (Bernabé, 1987). Bernabé found a decrease of α with confining pressure as a transition occurred between elastic deformation of the cracked solid in the low confining pressure region and local deformation processes controlled by indentation of asperities in the highest confining pressure region. Such a difference is likely to be due to the nature of the rock and may depend on its mineralogical composition.

Finally, a similar investigation of pressure dependent permeability turned out to be impossible with Sample No. 3 because of large scattering in the data and unusual behaviour during the experiments (e.g. permeability increase while increasing confining pressure). At 20 MPa confining pressure and 10 MPa pore pressure, we measured a permeability of 0.75 millidarcies. We think that during sample loading, stress gradients induced by the important heterogeneity of the porous structure may develop in the rock: consequently, an incoherent response in the deformation of the porous network should not be surprising. This last result emphasizes the importance of both heterogeneities and the scale of these heterogeneities.

3.4. ELECTRICAL MEASUREMENTS

Electrical conductivity measurements have been performed on the three above samples at room temperature and pressure conditions. Experiments at a fixed

frequency (4 kHz) were performed on the Fontainebleau Sandstone samples saturated with various potassium chloride water solutions of increasing strength. A useful representation is to plot in logarithmic coordinates the sample conductivity σ_r as a function of electrolyte conductivity σ_w (Figure 20). The general equation satisfied by the rock conductivity is:

$$\sigma_r = (1/F)\sigma_w + \sigma_s,$$

where F is the resistant formation factor and σ_s is the surface conductivity of the rock. In the low electrolyte conductivity region, surface conduction processes dominate and the rock conductivity approaches the constant value σ_s. By contrast, when $\sigma_w \gg \sigma_s$, surface conductivity is negligible and the rock conductivity is proportional to the electrolyte conductivity. Thus, such a conductivity plot provides both the surface conductivity term and the formation factor F related to bulk conduction processes in the porous network.

As expected, the formation factor correlates inversely with bulk porosity: we found $F = 30$ for Sample No. 1, $F = 100$ for Sample No. 2 and $F = 330$ for Sample No. 3. It is clear, however, that the high F increase cannot be explained by changes in the bulk values of porosity only, especially if one compares the data for Samples No. 2 and No. 3. If we study the shape of the conductivity curves, we see that the extension of the linear part in the high electrolyte conductivity range becomes larger as the sample porosity increases whereas the conductive properties of Sample No. 3 are highly influenced by surface conductivity over almost the whole range of the electrolyte strengths investigated. Although we could not observe the constant asymptotic value in the lower conductivity range for Sample No. 1, the following relation seems to be satisfied:

$$\sigma_{s(S1)} < \sigma_{s(S2)} < \sigma_{s(S3)}$$

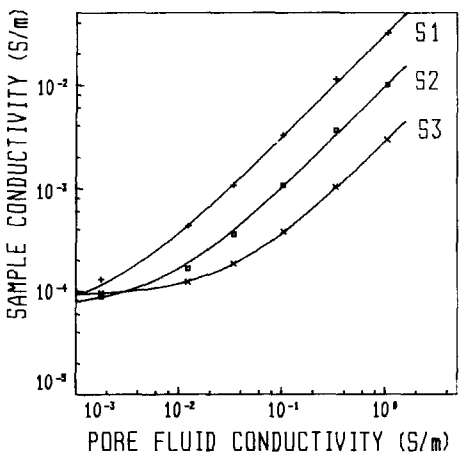

Fig. 20. Sample conductivity vs. pore fluid conductivity plot, samples Nos. 1, 2, and 3 saturated with KCl water solutions.

The surface conductivities for Sample No. 2 and Sample No. 3 are 7.0×10^{-5} S m^{-1} and 9.0×10^{-5} S m^{-1}, respectively. Thus surface conductivities correlate inversely with bulk conductivities; such a behaviour has been mentioned by Pape *et al.* (1984). The relative importance of surface conduction processes in porous rocks is controlled by the surface to volume ratio S/V of the pores: this ratio depends on the nature and local structure of porosity. For example, it is higher for crack-like pores than for equant pores. Furthermore, silicification is assumed to progressively fill the pore volume without significantly reducing the internal surface of the rock.

4. Relations Between Bulk Parameters

In Table I, we summarize the whole experimental data relative to the bulk properties of our samples.

Many authors have investigated the relations between permeability, formation factor and bulk porosity. The well-known relationship $F = \Phi^{-m}$, for example, states that formation factor F follows a power law, where m is the cementation exponent varying between 1.3 and 2.5 for a large assortment of rocks (Dullien, 1979). Using this simple formalism for our data, we found respectively $m_{(S1)} = 1.62$, $m_{(S2)} = 1.64$, and $m_{(S3)} = 1.95$, which fall inside the usual range.

Another way of relating the formation factor to porosity is to use the electrical tortuosity factor X_e defined by the relationship $F = X_e/\Phi$. By definition, X_e includes the effect of constrictions in the capillaries. Our experimental results on the Fontainebleau sandstone yield, respectively, $X_{e(S1)} = 4$, $X_{e(S2)} = 6$, and $X_{e(S3)} = 17$ which also fall within an acceptable range compared to data on other sandstones (Dullien, 1979).

The agreement between these two phenomenological approaches indicates a good consistency of our results. The somewhat different behaviour shown by sample No. 3 is emphasized by large values of both cementation exponent m and electrical tortuosity X_e. To explain this, we suggest that as silicification develops, it makes the conducting flow paths longer and significantly decreases the connectivity of the porous framework. In fact, the tortuosity factor can be well understood with the help of the percolation concept: a large tortuosity corresponds for example to a situation where pore connection is weak. In other words, although 'infinite clusters' as defined by the percolation theory, must exist through the medium in order to insure

Table I. Bulk properties of the Fontainebleau Sandstone samples.

Sample	S. No. 1	S. No. 2	S. No. 3
Porosity	12.3%	6.0%	5.1%
Permeability[a]	35 mD	2.5 mD	1.0 mD
Formation fact.	30	100	330

[a] Water permeabilities extrapolated to room conditions.

electrical and hydraulic conduction, there are only a few of them. Linking the tortuosity concept to the percolation theory is a fairly new approach as indicated by Gueguen and Dienes (1989).

5. Conclusions

In our experiments we observed that transport properties varied significantly from one sample to another, although all of them belonged to the same geological formation. However, changes in bulk porosity alone cannot explain the main features of the permeability and conductivity data. If this were the case, the value of the cementation exponent m would be the same for all the samples as the mineralogical content and grain size are constant in Fontainebleau sandstones. Consequently, microstructural parameters relative to the porous network have to be included in all detailed analysis on the transport properties of rocks. Thorough microstructure analysis of the porous network gives additional information for the interpretation of capillarity test curves. Confining pressure and pore pressure do not play symetrical roles during fluid flow measurements, particularly in the sample with crack-like pores. Surface conductivity effects are larger in the sample with a porous network composed of large pores connected by tiny channels. In addition, the variations of the electrical tortuosity factors (4 to 17) are corroborated by microstructure variations. Although there are different ways of taking microstructures into account, we think that it is necessary to go further; a promising approach is to quantify statistically the microstructural parameters by means of thin sections observations. In particular, the measurement of microstructural parameters such as the throat size distribution will provide the necessary figures for numerical simulations of statistical models on transport properties (David *et al.*, 1990; Gueguen and Dienes, 1989). Further comparison with direct measurements will enable to test the validity of the modeling.

Acknowledgements

The authors are grateful to Y. Gueguen for advice and helpfull discussions and to anonymous reviewers for their criticisms and suggestions. R. Wicker and B. Cantin are thanked for valuable assistance given during construction of apparatuses. This work has been supported by the AFME convention 9200012 and the CNRS-ARC 'Géothermie de roches sédimentaires'.

References

Bernabe, Y., 1987, The effective pressure law for permeability during pore pressure and confining pressure cycling of several crystalline rocks, *J. Geophys. Res. B.* **92**, 649–657.

Bernabe, Y., 1988, Comparison of the effective pressure law for permeability and resistivity formation factor in Chelmsford Granite, *Pageoph* **127**, 607–625.

Bourbie, T., Coussy, O., and Zinszner, B., 1986, *Acoustique des milieux poreux*, Technip éd., Paris.

Bousquie, P., 1979, Texture et porosité de roches calcaires, Thèse Ecole des Mines, Paris.

Brace, W. F., 1977, Permeability from resistivity and pore shape, *J. Geophys. Res.* **82**(23), 3343–3349.

Brace, W. F., 1980, Permeability of crystalline and argillaceous rocks, *Int. J. Rock Mech. Min. Sci. and Geomech. Abstr.* **17**, 241–251.

Brace, W. F. and Orange, A. S., 1968, Electrical resistivity changes in saturated rocks during fracture and frictional sliding, *J. Geophys. Res.* **73**, 1433–1445.

Brace, W. F., Orange, A. S., and Madden, T. R., 1965, The effect of pressure on the electrical resistivity of water saturated crystalline rocks, *J. Geophys. Res.* **70**(22), 5669–5678.

Brace, W. F., Walsh, J. B., and Frangos, W. T., 1968, Permeability of granite under high pressure, *J. Geophys. Res.* **73**(6), 2225–2236.

David, C., Gueguen, Y., and Pampoukis, G., 1990, Effective medium theory and network theory applied to the transport properties of rock, *J. Geophys. Res. B*, **95**(5) 6993–7005.

Daily, W. D. and Lin, W., 1985, Laboratory determined transport properties of Berea sandstone, *Geophysics* **50**(5), 775–784.

Doyen, P. M., 1988, Permeability, conductivity and pore geometry of sandstone, *J. Geophys. Res. B* **93**(7), 7729–7740.

Dullien, F. A. L. and Dhawan, G. K., 1974, Characterization of pore structure by combination of quantitative photomicrography and mercury porosimetry, *J. Colloïd Interface Sci.* **47**(2), 337–349.

Dullien, F. A. L., 1979, *Porous Media: Fluid Transport and Pore Structure*, Academic Press, New York.

Friedmann, M. G., 1958, Determination of sieve-size distribution from thin-sections data for sedimentary petrological studies, *J. Geol.* **66**, 394–416.

Gueguen, Y. and Dienes, J., 1989, Transport properties of rocks from statistics and percolation, *Math. Geol.* **21**(1), 1–13.

Mertz, J-D. 1989, Rôle des structures de porosité dans les propriétés de transport, Thèse U.L.P. Strasbourg.

Monicard, R. 1965, *Caractéristiques des roches réservoirs*, Cours de Production, Technip éd., Paris.

Nur, A. and Byerlee, J. D., 1971, An exact effective stress law for elastic deformation of rock with fluids, *J. Geophys. Res. B* **76**(26), 6414–6419.

Pape, H., Riepe, L., and Schopper, J. R., 1984, Calculating permeability from electrical logging data, *9th Int. Formation Evaluation Sympos. Trans.*, Paris, paper 22, 1–10.

Pickell, J. J., Swanson, B. F., and Hickman, W. B., 1966, Application of air-mercury and oil-air capillarity pressure data in the study of pore structure and fluid distribution, *SPE J.* 55–61.

Robin, P. Y. 1973 Note on effective pressure, *J. Geophys. Res. B*, **78**(14), 2434–2437.

Wardlaw, N. C., and Taylor, R. P., 1976, Mercury capillarity pressure curves and the interpretation of pore structure, *Bull. Canad. Petrol. Geol.* **24**, 225–262.

Zinszner, B. and Meynot, C., 1982, Visualisation des propriétés capillaires des roches réservoirs, *Rev. IFP Paris* **37**(3), 337–361.